SSRG International Journal of Electrical and Electronics Engineering
ISSN: 2348-8379/ https://doi.org/10.14445/23488379/IJEEE-V12I5P122

Volume 12 Issue 5, 261-277, May 2025

Original Article

Enhanced Power Quality with PV-Based DSTATCOM Using Cascaded Boost Converter and Neural Network Control Strategy

G. Lakshminarayana[1*], K. Kalaiyarasan[2], D. Sowmiya[3], V. P. Arumbu[4]

[1]*Department of Electrical and Electronics Engineering, VNR Vignana Jyothi Institute of Engineering and Technology, Hyderabad, India.*
[2]*Department of Electrical Engineering, Anna University, Chennai, India.*
[3]*Department of Electrical Engineering, Anna University, Chennai, India.*
[4]*Department of Electrical and Electronics Engineering, Sri Ramanujar Engineering College, Chennai, India.*

[*]*Corresponding Author : lakshminarayana_g@vnrvjiet.in*

Received: 18 March 2025 Revised: 23 April 2025 Accepted: 04 May 2025 Published: 31 May 2025

Abstract - *Climate conditions that cause Power Quality (PQ) issues greatly affect the electricity produced by Renewable Energy Sources (RES), such as Photovoltaic (PV) systems, which need quick adjustment of energy transmission and distribution systems. To mitigate reactive power compensation and lower voltages well, sag, and Total Harmonic Distortion (THD), the Distribution Static Synchronous Compensator (DSTATCOM) is exploited. The function of DSTATCOM is effectively managed by a Decoupled Neural Network (DNN) controller. The DSTATCOM receives the power from the PV system, and its voltage is enhanced by an improved cascaded boost converter. Furthermore, the Horse Held Optimization (HHO) based Fuzzy Maximum Power Point Tracking (MPPT) is employed to track peak power from the PV system. MATLAB/Simulink platform is employed to assess the validation of the developed DSTATCOM with the control method under the rated capacity of distribution generation. Finally, the findings in this research demonstrate the enhanced performance of PV-DSTATCOM while ensuring grid integration and improved PQ with Total Harmonic Distortion (THD) values of 1.10%, 0.71%, and 1.06%.*

Keywords *- DSTATCOM, DNN controller, PV system, Improved cascaded boost converter, HHO-based Fuzzy MPPT.*

1. Introduction

PQ problems are frequently produced by the use of sophisticated electronic equipment and load variations. A distribution system is increasingly experiencing issues with harmonic generation and voltage sag/swell [1]. Modern power electronics and computer-controlled equipment are examples of nonlinear loads that are becoming more and more common, which is the cause of these difficulties. These problems have the ability to harm sensitive equipment and result in expensive losses for electrical networks. Electrical equipment malfunctions and loads behave strangely when there is poor power quality. Recent advances in semiconductor technology have led to a large growth in the usage of nonlinear loads in distribution systems, raising concerns among researchers about PQ issues [2, 3]. In order to address PQ concerns, a variety of Flexible AC Transmission System (FACTS) controllers are also extensively integrated into the load [4, 5]. Thyristor-based and Voltage Source Inverter (VSI)-based FACTS controllers are the two primary types into which these controllers are usually divided [6]. To address the problems with PQ, the STATCOM is exploited as a shunt controller, injecting current into the line to regulate voltage at and around the point of connection, sustain power flow along pre-established pathways, and boost the line's transmission capacity [7]. However, a system that has STATCOM installed is unable to temporarily regulate the voltages in a real distribution and transmission system. Moreover, these STATCOMs are not equipped inherently to respond to short, rapid voltage fluctuations [8, 9]. Another FACTS device known as the Dynamic Voltage Restorer (DVR) compensates for voltage sags, swells, and voltage harmonics from loads. A distribution feeder uses DVR to safeguard the load against errors brought on by voltage sags and swells. DVRs reduce harmonics, but if they are not correctly designed and controlled, they potentially add additional harmonics to the system [10]. In order to accomplish transient-free switching and preserve power quality, a Thyristor binary switched capacitor is presented in [11]. However, because of thyristors' switching properties, BSCs are not appropriate for high-frequency applications. The responsiveness of BSCs gets limited and delays get introduced due to the slow switching ability. The Static VAR is represented in [12], and depending on the type of incoming circuit, a compensator is designed to either inject or absorb reactive power. SVCs reduce harmonics, but in some cases, they also produce harmonics that need further filtering.

In order to address power quality concerns brought on by nonlinear loads, a DSTATCOM, an interface device between solar PV systems and the load, is developed in this research. Power quality concerns, including phase imbalance, reactive power burden, and harmonics, are addressed by connecting solar PV installations to the grid through DSTATCOM. Due to its abundance and ability to provide pollution-free energy, solar energy has emerged as the most popular renewable energy source for power generation [13, 14]. Boost converters [15] and cascaded boost converters [16] are DC-DC converters that have been effectively used to increase the PV system output, which is often reduced as a result of operating conditions [17]. However, these converters have higher output voltage ripple, high peak current, and lower efficiency. To overcome such issues, this research develops an improved cascaded boost converter to enhance the voltage of the PV system. MPPT approaches, such as Perturb and Observe (P&O) [18] and Incremental Conductance [19], are employed to track peak power from PV systems [20]. The slow convergence, fixed perturbation steps, limited efficiency in dynamic situations, and oscillation around the endpoint are some of the disadvantages of these approaches. Particle Swarm Optimization (PSO) [21], the Jaya optimization method [22], and Ant Colony Optimization (ACO) [23] are examples of optimization algorithms that have acquired prominence recently; however, they are complicated by their enormous population-sized data. Finally, this research implements a Fuzzy MPPT controller, and its parameters are tuned by Horse held optimization algorithm.

Although various FACTS devices exist, they face certain drawbacks, including restricted dynamic response, additional harmonics, and unsuitability for high-frequency applications. Also, conventional converters exhibit reduced efficiency, high voltage ripple, and increased peak currents. Existing MPPT approaches struggle with poor performance and slow convergence under dynamic conditions. Hence, there exists a need for an integrated system to enhance voltage levels, improve power quality, and efficiently extract maximum power from PV systems. A novelty of the proposed work lies in the integration of an Improved Cascaded Boost converter with HHO based Fuzzy MPPT controller in D-STATCOM. Additionally, DNN is employed for effective control, thereby enhancing power quality. The proposed converter offers improved voltage gain with reduced output ripple when compared to conventional converters. The MPPT approach provides better convergence and adaptability, whereas DNN offers superior real-time control performance compared to classical approaches.

The key motivations of this research are,

- To enhance the power quality, a D-STATCOM is implemented, which regulates the reactive power and voltage.
- Implementing an improved cascaded boost converter enhances the low voltage of the PV system.
- The HHO-based fuzzy MPPT controller is used to track the maximum power from the PV system, and the horse-held optimization method enhances its performance.

2. Proposed Methodology

The developed research incorporates DSTATCOM with an improved cascaded boost converter to alleviate PQ issues. Figure 1 illustrates an advanced power system that incorporates a PV system with a grid-connected distribution network for proficient power management and enhanced system stability. Initially, power electronics-based loads are used in power systems that are fed by 3ϕ AC source, encountering source impedance with inductance and resistance. If these power quality problems are not addressed, they impact voltage stability and lead to equipment failure, power losses, and a decrease in power factor.

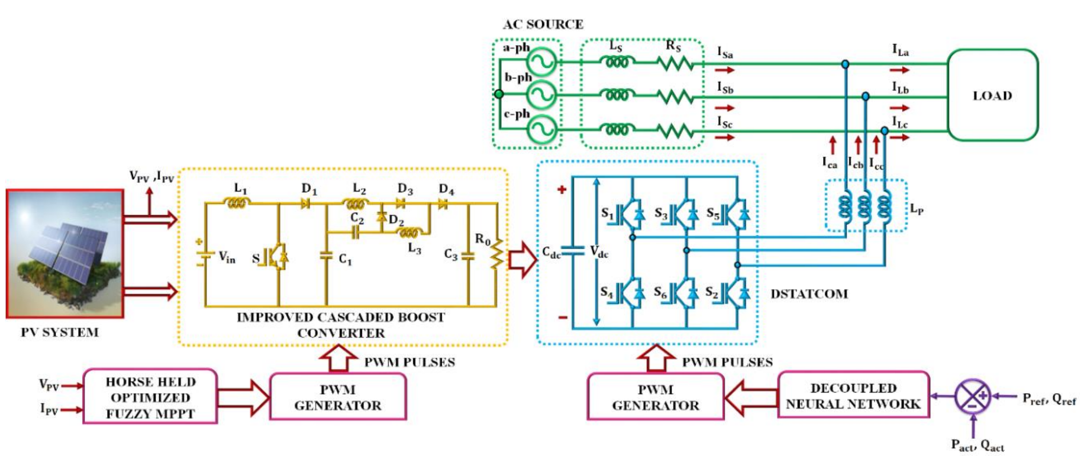

Fig. 1 Block diagram of PV-based DSTATCOM

Therefore, this research develops a DSTATCOM that offers reactive power compensation and voltage regulation to enhance power quality. It receives DC power from the improved cascaded boost converter and absorbs or injects reactive power into the grid depending on system demands. Here, the low voltage of the PV system is enhanced by utilizing an improved cascaded boost converter. After that, the peak power of the PV system is tracked by using a Fuzzy MPPT controller, which is optimized with the aid of Horse held optimization algorithm. Subsequently, the produced PWM pulses from the PWM generator are exploited to improve the operation of the developed converter. To control the real and reactive power, the system integrates a decoupled neural network, which generates the control signals for DSTATCOM. Then, the PWM generator develops PWM pulses for better functioning of DSTATCOM. Furthermore, it is attached to a load through a transformer, allowing power transfer and voltage level adaptation to meet the requirements of the load, ensuring enhanced power quality and reliability.

2.1. DSTATCOM

When load balancing, mitigation of harmonic current and compensation of reactive current are essential in an AC distribution system, a DSTATCOM is a device that is utilized. The main part of a DSTATCOM is a Voltage Source Converter (VSC), which is composed of a capacitor on a DC bus and self-commutating semiconductor valves. A device is a shunt connected to a power distribution network via a coupling inductance, which is usually accomplished by the transformer leaking reactance. DSTATCOM offers load balancing, harmonic compensation, and power factor correction. Since steady-state reactive power generation does not depend on the size of the capacitor, the total size and cost of the compensator are diminished. The diagram of a DSTATCOM supplying three-phase loads via a three-phase AC main is displayed in Figure 2. Three-phase loads are nonlinear, imbalanced, trailing power factor, or a combination of these loads. Interfacing inductors (L_f) are utilized at the AC side of the VSC to reduce ripple in compensating currents. A ripple filter, which is positioned at PCC in parallel with the loads and compensator to filter voltage's high-frequency switching noise, is represented by a small series linked capacitor (C_f) and resistor(R_f).The DSTATCOM introduces the harmonics/reactive currents (i_{cabc}) to terminate the load current's reactive power and harmonics component, resulting in compensated load reactive power and harmonic-free source currents. The necessary compensation's voltage and current ratings serve as the basis for the switches' ratings. The selection of the DSTATCOM ripple filter, DC bus capacitor, voltage, and AC inductors are described below,

2.1.1. DC Bus Voltage

For PWM management of the VSC of DSTATCOM, the DC bus voltage(V_{dc}), which is dependent on PCC voltage, is bigger than the amplitude of the AC voltage. V_{dc} for a three-phase VSC is determined by,

$$V_{dc} = {}^{2\sqrt{2}V_{LL}}\Big/_{(\sqrt{3}m)} \tag{1}$$

Where m is the modulation index and V_{LL} is the DSTATCOM's AC line output voltage.

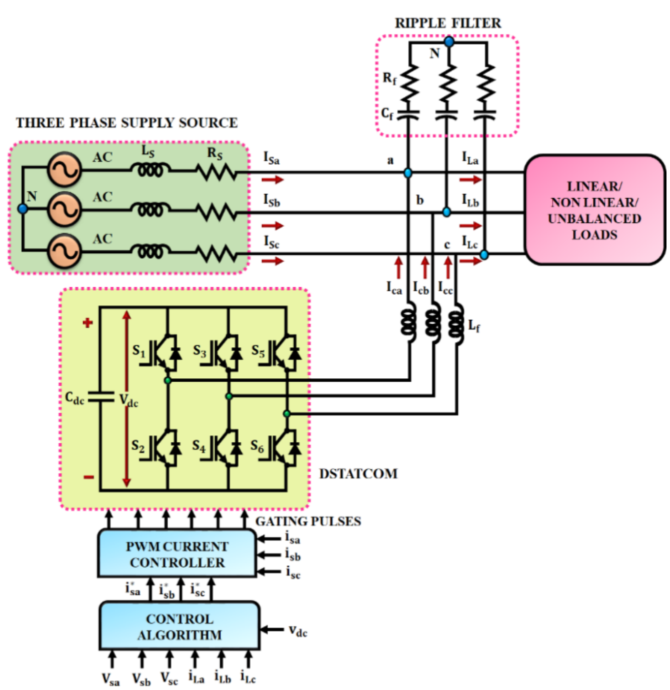

Fig. 2 Schematic diagram of DSTATCOM

2.1.2. DC Bus Capacitor

When loads are applied, the V_{dc} decreases, and when the loads are removed, the V_{dc} increases, which determines the DC bus capacitor design. The formula that governs C_{dc} using the energy conservation principle is,

$$0.5C_{dc}\{(V_{dc}{}^2) - (V_{dc1}{}^2)\} = k\{3V_{ph}(a\,I)t\} \tag{2}$$

Where V_{dc} is the nominal DC voltage, V_{dc1} is the DC bus's least voltage level, a is the overloading factor, V_{ph} is the voltage of phase, I is the current of VSC's phase, and t is the amount of time needed to recover theV_{dc}.

2.1.3. AC Inductor

The ripple currenti_{crpp} and switching frequency f_s all influence the selection of AC inductance. The AC inductance is,

$$L_f = \sqrt{3}mV_{dc}/\{12 * a * f_s * i_{crpp}\} \tag{3}$$

2.1.4. Ripple Filter

Using a first-order high pass filter set at half of the ef_s, the high-frequency noise is eliminated from the voltage at PCC. A capacitor with series resistance is selected to act as a ripple filter. High impedance at the fundamental frequency and low impedance at half of the $f_s$are features of this filter that allow high-frequency noises to pass over the ripple filter branch at frequencies greater than the fundamental frequency while blocking the fundamental component's flow at the fundamental frequency. The function of DSTATCOM is managed by a DNN controller.

2.2. Decoupled Neural Network Controller

Incorporating a DNN controller in DSTATCOM enhances the performance of the DSTATCOM system. The DNN is utilized for complex nonlinear system dynamics and simplifies the control design by defining separate sliding surfaces for each subsystem, as shown in Figure 3.

$$s_1 = c_1(x_1 - z) + x_2 = [c_1 1][x_1 \quad x_2]^T - c_1 z = c^T X_{12} - c_1 z \tag{4}$$

Another switching line is,

$$s_2 = c_2 x_3 + x_4 \tag{5}$$

To preserve the states on the sliding surface, an equivalent control is first provided in the decoupled controller design. A stable control system is obtained in sliding motion, and the system dynamic is unrelated to the original system. By setting s_1 to zero, the equivalent control is achieved.

$$\dot{s_1} = c_1(\dot{x_1} - \dot{z}) + \dot{x_2} = c_1 x_2 - c_1\dot{z} + f_1 + b_1 u + d_1 = 0 \tag{6}$$

The input is selected as below for a Lyapunov function candidate,

$$V = \frac{1}{2}s_1 s_1^2 \tag{7}$$

The time derivative of expression (7),

$$\dot{V} = s_1\dot{s_1} = s_1(c_1 x_2 - c_1\dot{z} + f_1 + b_1 u + d_1) \tag{8}$$

The controller is split into a control input of equivalent and a reaching mode, which is negative, as expression (8).

$$u = u_{eq} - M.sgn(s_1/\Phi_1),\ Where\ M > D_1(t)/|b_1(t)| \tag{9}$$

The system is regulated so that the state approaches and strikes the sliding surface when M is a positive constant. As a result, the trajectory is always transferred in the direction of the sliding surface. However, because of the "sgn" function, expression (9) has high-frequency switching close to the sliding surface ($s_1 = 0$). Therefore, $sat(s_1)$with $sgn(s_1)$ is replaced in the following way to lessen the chattering phenomenon.

$$u = u_{eq} - M.sat(s_1) \tag{10}$$

In the sliding motion, an equivalent controller is,

$$u_{eq} = \frac{1}{b_1}(-c_1 x_2 + c_1\dot{z} - f_1 + \dot{s}_1 + ks_1) \tag{11}$$

Substituting expression (11) into (6),

$$\dot{s}_1 + ks_1 = 0$$

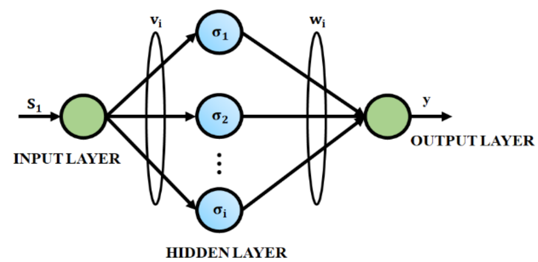

Fig. 3 Structure of DNN

The goal of control is to return the system state to its initial condition of equilibrium. An intermediate variable z gradually simultaneously reduces the switching line variables s_1 and s_2 to zeros. According to expression (4), the control aim of u_1 is now $x_1 = z, x_2 = 0$instead of$x_1 = 0, x_2 = 0$. Since the entire system is controlled by the controller $u = u_1$, the bound of $x_1$is ensured by letting,

$$|z| \le z_{upper}, 0 < z_{upper} < 1 \tag{12}$$

Where$z_{upper}$is the$abs(z)$'s upper bound. Expression (12) denotes that the x_1's maximum absolute value is restricted.

$$z = sat(s_2/\Phi_z).z_{upper}, 0 < z_{upper} < 1 \tag{13}$$

Wheres_2's boundary layer is $\Phi_z$to smooth$z$, $\Phi_z$shifts s_2 to the appropriate range ofx_1 and $sat(.)$ function is,

$$sat(\varphi) = \begin{cases} sgn(\varphi) & if|\varphi| \geq 1 \\ \varphi & if|\varphi| < 1 \end{cases} \tag{14}$$

Where, $z_{upper}$is a factor, and z is a decaying oscillation signal.DNNs are employed to approximate unknown nonlinear functions in $f(x)$ and $b(x)$. It contains input, hidden, and output layers with weights $\widehat{\omega}$ and $\hat{v}$ that is adaptively updated,

$$f(x) \approx \widehat{\omega}^T \sigma(\hat{v}^T x) \tag{15}$$

Where, $\sigma(.)$is a nonlinear activation function, and updated weights are $\widehat{\omega}$ and $\hat{v}$. The adaptive laws is derived from Lyapunov theory to ensure stability,

$$\dot{\widehat{\omega}} = -\eta_1 s_1 \sigma(x) \tag{16}$$

$$\dot{\hat{v}} = -\eta_2 s_1 \sigma'(x) \widehat{\omega} \tag{17}$$

Here,η_1 and η_2 are learning rates managing weight adjustments. The DNN-based controller dynamically adjusts the reactive power injected or absorbed by the DSTATCOM. By developing compensating currents, the DNN calculates and cancels nonlinear distortions from the load, resulting in harmonic-free source currents. The decoupled neural network-based control of DSTATCOM delivers an effective solution for addressing modern power quality issues. It ensures robust performance, real-time adaptation, and precise regulation of currents and voltages in distribution networks.

2.3. PV System

Using a single-diode model, the basic structure of a solar cell is determined. To obtain the required voltages, a PV array's modules are commonly connected in series before the individual components are connected in parallel. Figure 4 displays the PV cell's circuit diagram. The following equation is obtained by applying Kirchhoff's law to the node,

$$I_{PV} = I_D + I_{sh} + I \tag{18}$$

The PV current equation is,

$$I = I_{PV} - I_{sh} - I_D \tag{19}$$

$$I = I_{PV} - I_O.\left[exp\left(V + I.\frac{R_S}{V_T}\right) - 1\right] - \left[V + I.\frac{R_S}{R_{sh}}\right] \tag{20}$$

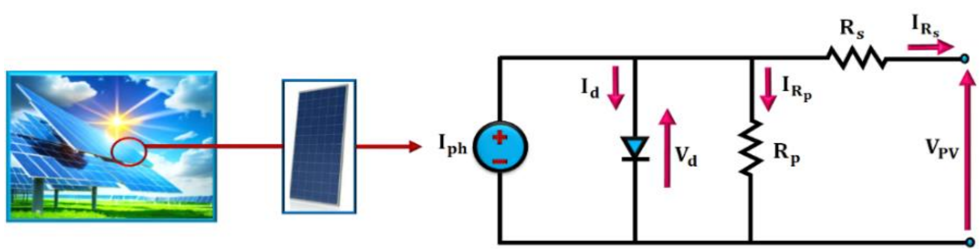

Fig. 4 Circuit of PV system

The insolation current is represented byI_{PV}, the cell current is$I$, the reverse saturation current isI_O, the cell voltage is V, and the series resistance isR_S. The shunt resistance is still needed to balance the isolation current, as indicated by Expression 2, based on the cell current. The parallel resistance isR_{sh}, thermal voltage isV_T, Boltzmann constant is$K$, the temperature is T, and electron charge is$q$. The improved cascaded boost converter, which raises the PV panel's voltage, is described in depth in the below section.

2.4. Improved Cascaded Boost Converter

Figure 5 shows the improved cascaded boost converter. It combines a quadratic boost cell with a conventional boost converter.

The circuit's three inductors are utilized to increase the voltage during operations. This circuit has two operational modes: on-state and off-state. Both modes are under CCM, which is very stable and simple to analyze.

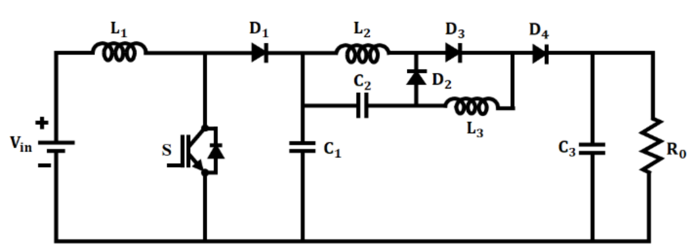

Fig. 5 Improved cascaded boost converter

2.4.1. Mode I

In mode 1, the switch S is turned on, and the input voltage is used to charge L_1. The capacitorC_1 charges the quadratic cell inductorL_2 and both C_1 and C_2 charge the inductor L_3. The output capacitor C_3charges the load.

$$V_{L1} = V_{in} \tag{21}$$

$$V_{L2} = V_{C1} \tag{22}$$

$$V_{L3} = V_{C1} + V_{C2} \tag{23}$$

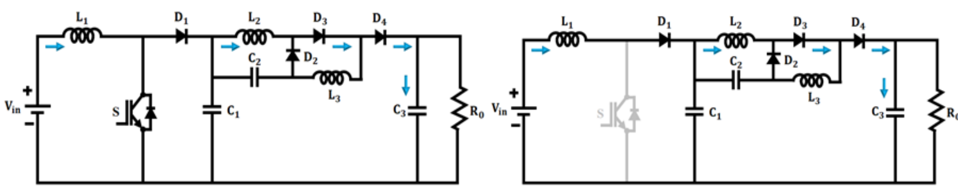

Fig. 6 Stages of developed converter

2.4.2. Mode II

In this mode, the switch S is inactive, and three inductors are discharged. A high current is sent to the load as a consequence of the input voltage and the three inductors discharging in series. Consequently, a high level of output voltage is generated. In this step, the input voltage and inductor L_1charge the capacitorC_1. L_2Charges the output capacitor C_3 and the load charges the output capacitor C_2 in parallel. The functional waveform of the developed converter is revealed in Figure 7.

$$V'_{L1} = V_{L1} \times \frac{D}{1-D} \tag{24}$$

$$V'_{L2} = V_{L2} \times \frac{D}{1-D} \tag{25}$$

$$V'_{L3} = V_{L3} \times \frac{D}{1-D} \tag{26}$$

$$V'_{C2} = V_{C2} = V'_{L2} \tag{27}$$

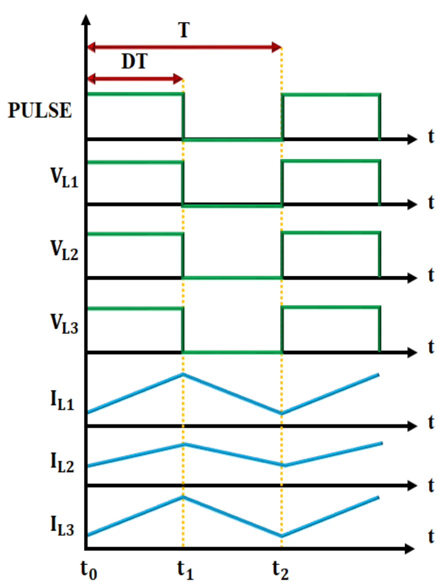

Fig. 7 Switching waveform of converter

$$V'_{C1} = V_{C1} = V_{in} + V'_{L1} \tag{28}$$

$$V_{out} = V_{in} + V'_{L1} + V'_{L2} + V'_{L3} \tag{29}$$

The relationship among voltage gain and the duty cycle is,

$$\frac{V_{out}}{V_{in}} = \frac{1}{(1-D)^3} \tag{30}$$

The maximum power from the PV system is tracked by exploiting Fuzzy MPPT, and its performance is improved by the HHO algorithm.

2.5. Horse Herd Optimized Fuzzy MPPT

One technique for managing the MPPT and determining the peak power point is fuzzy logic theory. The fuzzy theory deals with uncertainty and inaccuracy regarding the MPP of solar PV panels because of variations in load and solar irradiation. As illustrated in Figure 8, the fuzzy logic membership function has one output rule and two input rules. Fuzzification, fuzzy inference, and de-fuzzification are further subcategories of the fuzzy control technique.

2.5.1. Fuzzification

The transition from real to fuzzy variables is made possible via fuzzification. Continuous measurements of the PV generator's real voltage (V) and current (I) allow for the calculation of power. When two requirements pertaining to 2 input variables of the controller are error E, which denotes the slope of the $P-I$ characteristic, and change of this error $(CE)$are satisfied at a sampling instant K, the control is established. The expression for variables E and CE is,

$$E(K) = \frac{P(K)-P(K-1)}{I(K)-I(K-1)} \tag{31}$$

$$CE(K) = E(K) - E(K-1) \tag{32}$$

Where$P(K)$ and $I(K)$denote the PV generator's power and current. The input $CE(K)$indicates displacement direction of the operating point at$K$, whereas the input $E(K)$indicates whether it is on the right or left of the MPP on the $P-I$ characteristic. An output of the developed controller is the shift in the duty ratio of the developed converter. To return an operation point to the best position where the slope is 0, the control is accomplished by regulating this duty ratio in accordance with the slope $E(K)$. Figure 8 illustrates that the fuzzy controller's input variables (E, CE) are obtained from the real signals (e, ce) by multiplying them by the relevant scale gains (S_E, S_{CE}). Then, using a basic fuzzy subset, they are transformed into linguistic variables like $PB, PS, Z0, NS\ and\ NB$.

2.5.2. Inference Engine

To find the output of fuzzy, the inference engine uses the rules to input fuzzy (developed from the process of fuzzification. To determine the corresponding linguistic values and the extent to which each component of the antecedent has been fulfilled for each rule, the input crisp values are fuzzified before the rules are evaluated. By altering the duty ratio according to an operating point's distance from the MPP, the rules primarily aim to bring an operating point closer to the MPP. If an operating point is far from MPP, the duty ratio is greatly increased or decreased.

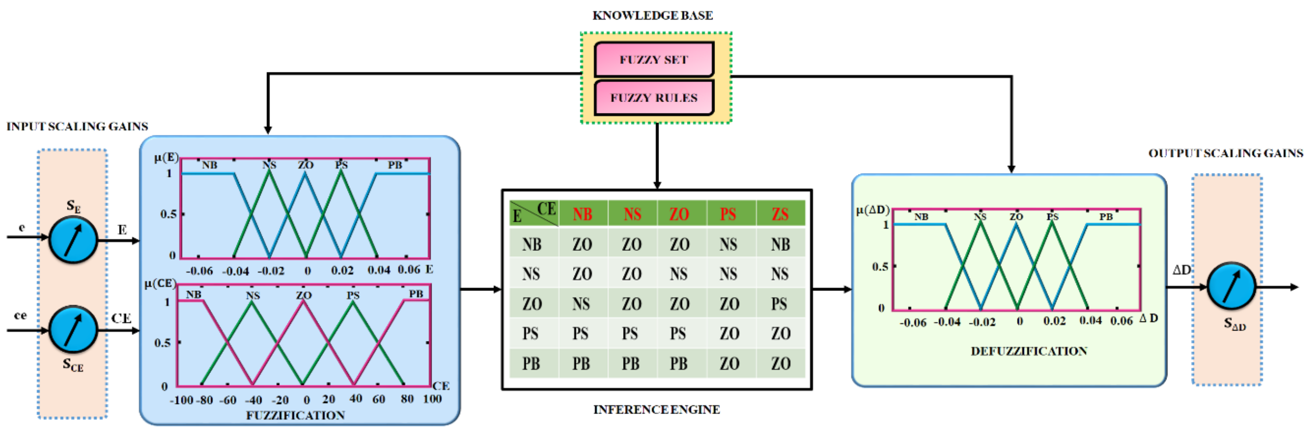

Fig. 8 Structure of FLC

2.5.3. Defuzzification

It is observed that the inference methods work on fuzzy information by providing a resulting membership variable function. It is necessary to envision a translation of this fuzzy data into predictable data, known as defuzzification because the converter needs an exact control signal D at its input. The center of gravity for a representation of sampled data is calculated by,

$$\Delta D = \frac{\sum_{j=1}^{n} \mu(\Delta D_j).\Delta D_j}{\sum_{j=1}^{n} \mu(\Delta D_j)} \tag{33}$$

Following defuzzification by expression (33) and scaling by the gain $S_{\Delta D}$, the fuzzy controller output, which is the change in duty ratio (K), is transformed into the actual duty ratio $D(K)$ by:

$$D(K) = D(K-1) + S_{\Delta D}.\Delta D(K) \tag{34}$$

Thus, the fuzzy MPPT controller is an effective approach to tracking the peak power from PV systems, and its performance is enhanced by the HHO algorithm. The HHO algorithm addresses issues in attaining the global maxima during nonlinear PV output caused by shading. The HHO algorithm improves fuzzy MPPT by optimizing the initialization and updating of the search space. The algorithm dynamically adjusts the searching parameters to explore and exploit the P-V curve, avoiding local maxima.

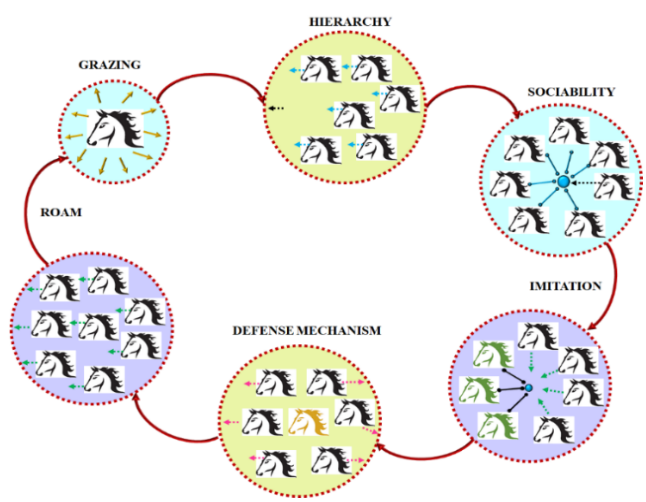

Fig. 9 Mechanism of HHO

2.5.4. Grazing

The HHO approach is exploited to denote the grazing space of each horse. Each horse grazes in particular locations as of the coefficient g. Horses graze throughout their lives, regardless of age.

$$Gra_m^{iter,age} = g_{iter}(low + r * upp)\left(P_m^{(iter-1)}\right),\ age = \alpha,\beta,\gamma,\delta \quad (35)$$

$$g_m^{iter,age} = \omega_g \times g_m^{(iter-1),age} \quad (36)$$

In this case, $Gra_m^{iter,age}$ indicates the ith horse's parameter of motion. With each iteration, the grazing variable diminishes linearly atω_g. The variables "low" and "upp" represent the bottom and grazing area's upper limits, and r is an arbitrary value between 0 and 1.

2.5.5. Hierarchy

The coefficient h_m in HHO, which is the tendency of a group of horses to follow the lead of the strongest and best-trained horse. Therefore, research has shown that horses obey the law of hierarchy while they are between the ages of 5 and 15 years or the middle ages of β and γ.

$$H_m^{iter,age} = h_m^{iter,age}\left(P_{lbh}^{(iter-1)} - P_m^{(iter-1)}\right) \quad (37)$$

$$h_m^{iter,age} = h_m^{(-1+iter),age} \times \omega_h \quad (38)$$

Here, $H_m^{iter,age}$shows where the best horse is located using the velocity variable. The best horse's position is indicated by the$P_{lbh}^{(iter-1)}$.

2.5.6. Sociability (Soc)

As shown in Figure 9, this behavior is represented by elements as a movement in the direction of other horses' typical locations.

$$SOC_m^{iter,age} = SOC_m^{iter,age}\left[\left(\frac{1}{N}\sum_{j=1}^{N} P_j^{(-1+iter)}\right) - P_m^{(-1+iter)}\right] age = \beta,\gamma \quad (39)$$

$$SOC_m^{iter,age} = SOC_m^{(-1+iter),age} \times \omega_{SOC} \quad (40)$$

The social motion vector that the ith horse is described by $SOC_m^{iter,age}$. $SOC_m^{iter,age}$indicates the horse's affinity toward i^{th}group. $iter$, which has a parameter of ω_S and is reduced in each cycle. An entire number of horses is denoted by N.

2.5.7. Imitation

Horses imitate one another, learning from each other's habits, including where to graze. Horses' imitation behavior is also considered a factor I in the current approach. Throughout their lives, young horses have apropensity to mimic their elders, as indicated in Figure 9.

$$Im_m^{iter,age} = im_m^{iter,age}\left[\left(\frac{1}{pN}\sum_{j=1}^{pN} P_j^{(-1+iter)}\right) - P^{(-1+iter)}\right] age = \gamma \quad (41)$$

$$Im_m^{iter,age} = im_m^{(-1+iter),age} \times \omega_{im} \quad (42)$$

A vector of motion demonstrating the i^{th} horse around an average of the best horse at position p is expressed by the$Im_m^{iter,age}$. On i^{th}iteration, $im_m^{iter,age}$ indicates a horse's attitude toward the group. Every cycle, this is decreased using the ωim parameter. Where p is 10% of the chosen horses,pN is the number of horses in the best positions. ω_{im} is a reduction factor per cycle for $iiter$.

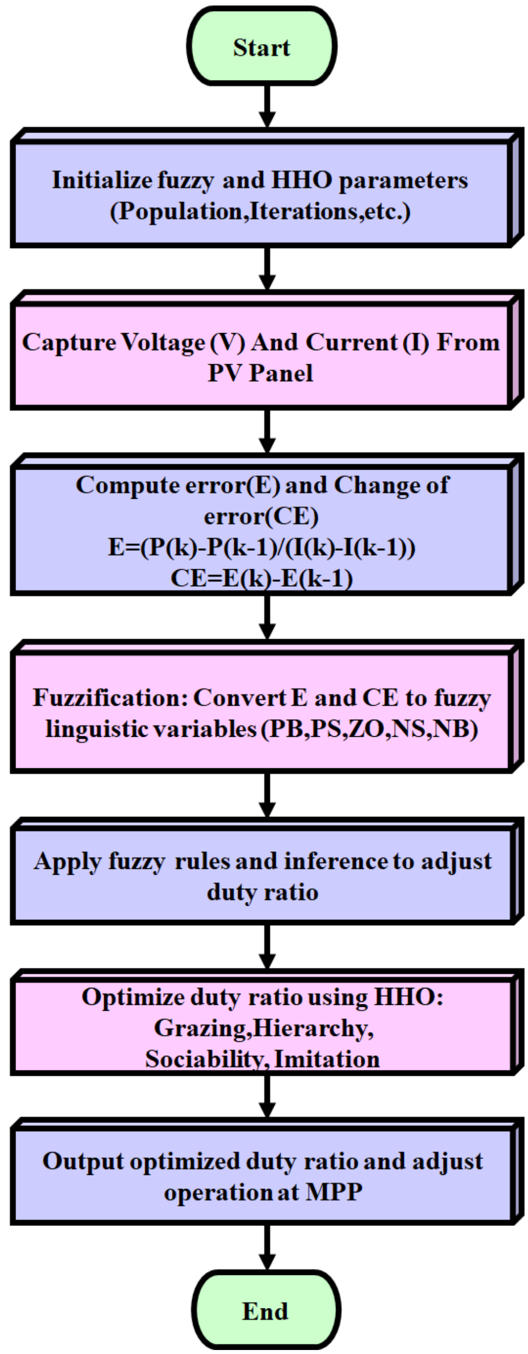

Fig. 10 Flowchart of Horse herd optimized fuzzy MPPT Defense Mechanism

The horses' defensive strategy includes running away from horses that behave indecorously. Horses have to fight their enemies or flee from them, as said earlier. When feasible, a horse's protective system is present at every stage of its existence.

Expressions (43) and (44) show that the horse's protective mechanism, which keeps the animal away from hazardous circumstances, is represented by a negative coefficient.

$$DefMec_m^{iter,age} = defmec_m^{iter,age}\left[\left(\frac{1}{qN}\sum_{j=1}^{qN} P_j^{(-1+iter)}\right) - P^{(-1+iter)}\right]; age = \alpha, \beta, \gamma \quad (43)$$

$$defmec_m^{iter,age} = defmec_m^{(-1+iter),age} \times \omega_{defmec} \quad (44)$$

$DefMec_m^{iter,age}$ defines the escape vector of the i^{th} horse. With q representing 20% of the entire number of horses, qN indicates the number of horses in the poorest situations. ω_{defmec} stands for the reduction factor per cycle for $iIter$.

2.5.5. Roam

Horses almost never roam when they are young, and as they get older, this behavior gradually diminishes. The roam variables are shown in expressions (45) and (46). Figure 10 shows the Horse herd-optimized fuzzy MPPT's flowchart.

$$RO_m^{iter,age} = ro_m^{iter,age} \partial P^{(-1+iter)} \quad age = \gamma, \delta \quad (45)$$

$$ro_m^{iter,age} = ro_m^{(-1+iter),age} \times \omega_{ro} \quad (46)$$

In this case, the ith horse's arbitrary velocity vector for a local area search and escape from local minima is $RO_m^{iter,age}$: For each cycle, ω_{ro} is a reduction factor of $ro_m^{iter,age}$.

The combined velocity vector is exploited to update the position of each horse, ensuring effective convergence toward the MPP. The tracking behavior of HHO is demonstrated using the duty cycle (dc) and the transient value of the output voltage.

In the upper right corner of the partially shaded power-voltage curve, there is only one point called Global Maxima (GM), with the other three points being Local Maxima (LM).

Increasing or reducing the number of horses has an influence on the PV system's efficacy; consequently, four horses are employed in this case to get good performance from the HHO. The power magnitude is used to calculate each horse's fitness. The movement of a horse is determined by its matching power at a specific location.

Algorithm for HHO

Initialize $max_{iter}, N, P_m, \omega_h, \omega_g, \omega_{SOC}, \omega_{ro}, \omega_{im}$
Evaluate the fitness of each horse
For each horse m in N
Measure V and I from the PV panel
Compute $P = V * I$
Set $fitness_m = P$
For $iter = 1$ to max_{iter}
Identify P_{best}, P_{worst}
For each horse m in N
Compute movement components and update position
Apply Fuzzy logic controller:
Capture V, I and calculate P
Compute error E and change of error CE
Fuzzify E and CE to linguistic variables
Apply fuzzy inference rules to adjust ΔD
Defuzzify to get a change in duty ratio
Adjust duty ratio using Equation (34)
Use a new position to refine $D(k)$
Evaluate new fitness of horse m using new duty cycle
Measure V, I and calculate P
Return best horse position as optimized duty cycle
End

3. Result and Discussions

This section analyses the outcomes of developed PV-based DSTATCOM for enhancing the power quality. In order to verify the developed work's efficacy, the comparative analysis is included in this part. The parameters of developed research are represented in Table 1.

Table 1. Specification of parameters

Parameter	Specification
AC Source	
Load Resistance	100Ω
Load Inductance	10mH
PV system	
Voltage (Open circuit)	22.6V
Voltage (Short circuit)	12V
Improved cascaded boost converter	
L_1, L_2, L_3	$4.7\ mH$
C_1, C_2	$22\ \mu F$
C_3	$2200\mu F$
Switching Frequency	10 kHz

3.1. Case 1: Constant Temperature and Irradiance

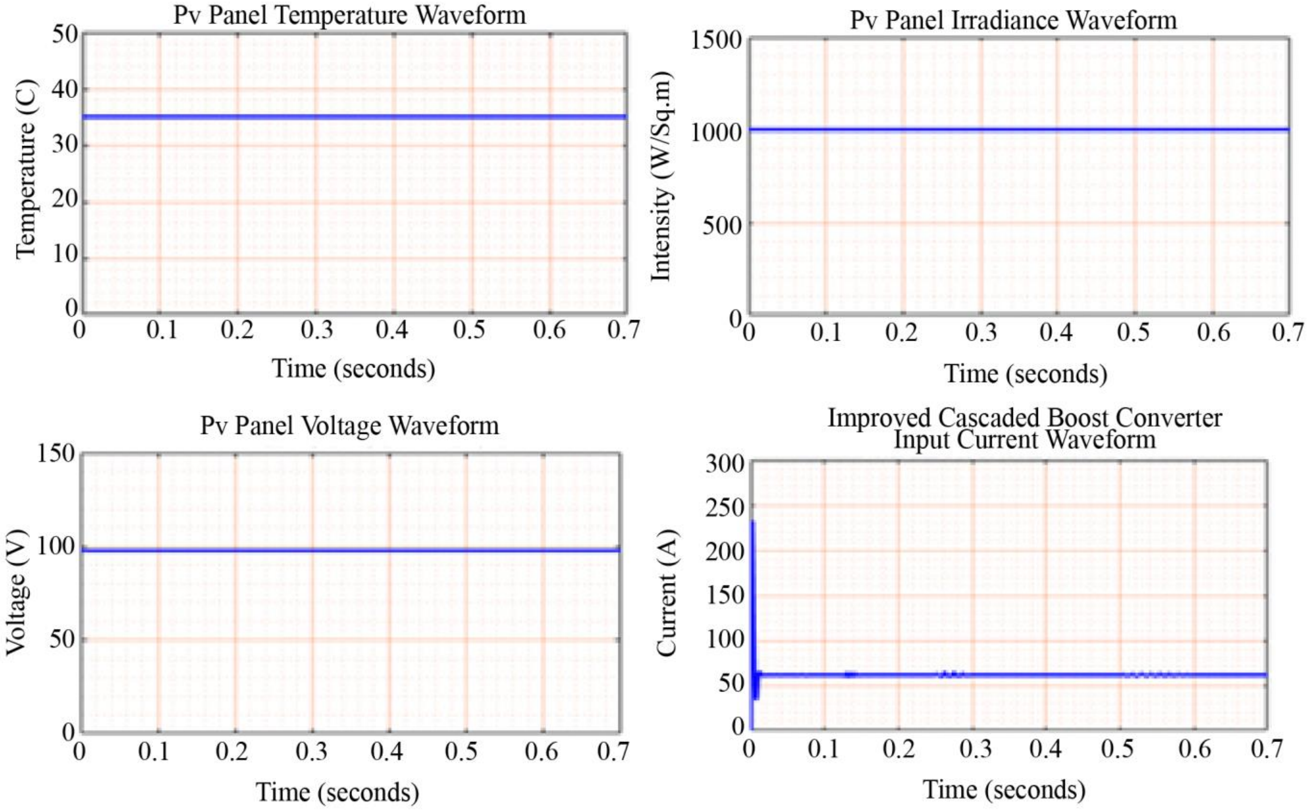

Fig. 11 Behaviour of solar panel

The behaviour of solar panels for constant temperature and irradiance conditions is indicated in Figure 11. The temperature is sustained at $35\,^{\circ}\mathrm{C}$, and the irradiance is maintained at $1000(W/Sq.m)$ in an entire system. Subsequently, voltage is sustained at a constant value of 95 V throughout the system. Additionally, the current varies in the starting stage and maintains a value of 60 A with small distortions.

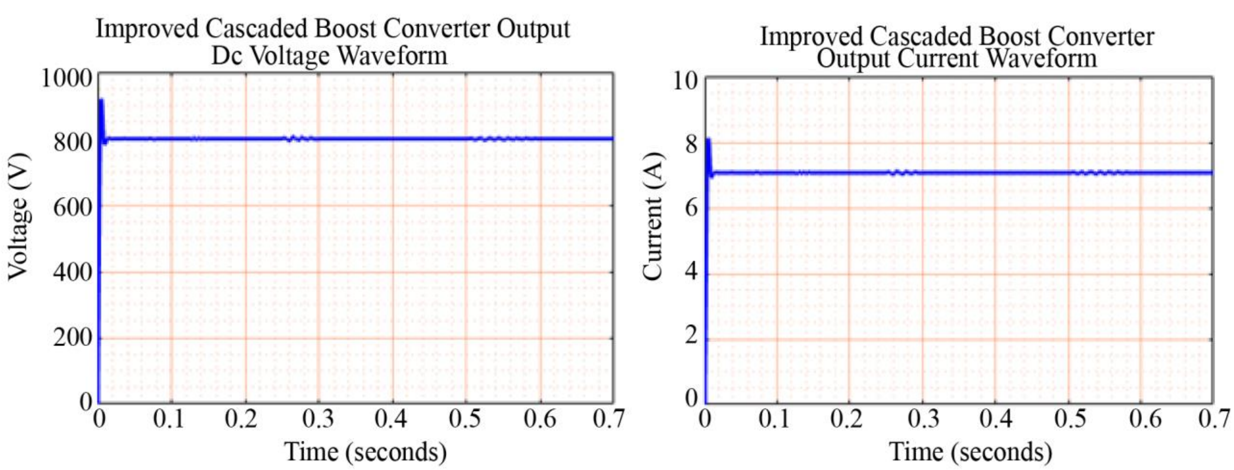

Fig. 12 Waveform of developed converter

Initially, the voltage of the converter is changed, and it sustained a stable value of 800 V with less oscillations. Also, the current output current is randomly varied in the initial period, and it maintained a value of 7A with little variations, as revealed in Figure 12.

3.2. Case 2: Varying Temperature and Irradiance

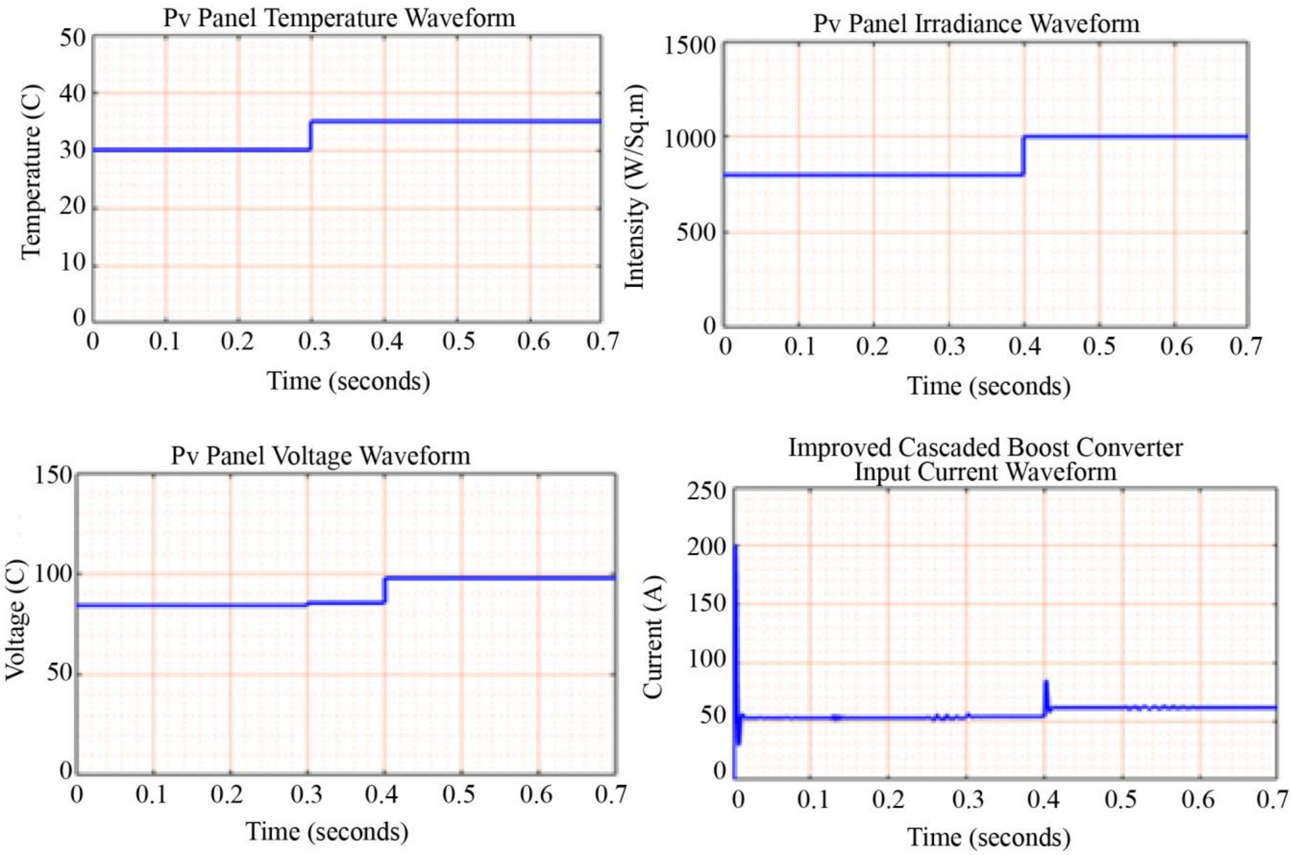

Fig. 13 Characteristics of solar panel

Figure 13 displays the characteristics of solar panels for varying irradiance and temperature conditions. At the starting stage, the temperature is varied, and then, it maintained a value of 35 ℃. Likewise, the irradiance is changed in the initial time, and it is sustained at a value of $1000(W/Sq.m)$. The voltage of the solar panel is gradually increased, and it settles at a value of 95 V without any distortions. Additionally, an input current steadily increases and is maintained at 60 A with just minor variations.

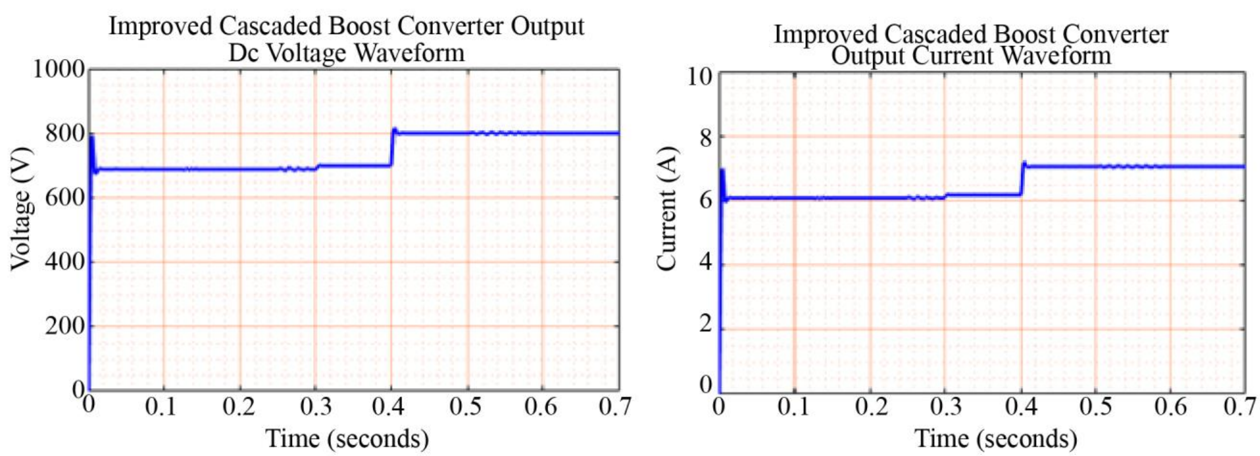

Fig. 14 Waveform of developed converter

Figure 14 shows the generated converter's waveform. After being originally adjusted, the output voltage settled at 800 V with only minor variations. Likewise, the output current is sustained at a value of 7A with small variations.

3.3. Case 1: Grid power (20 kW)

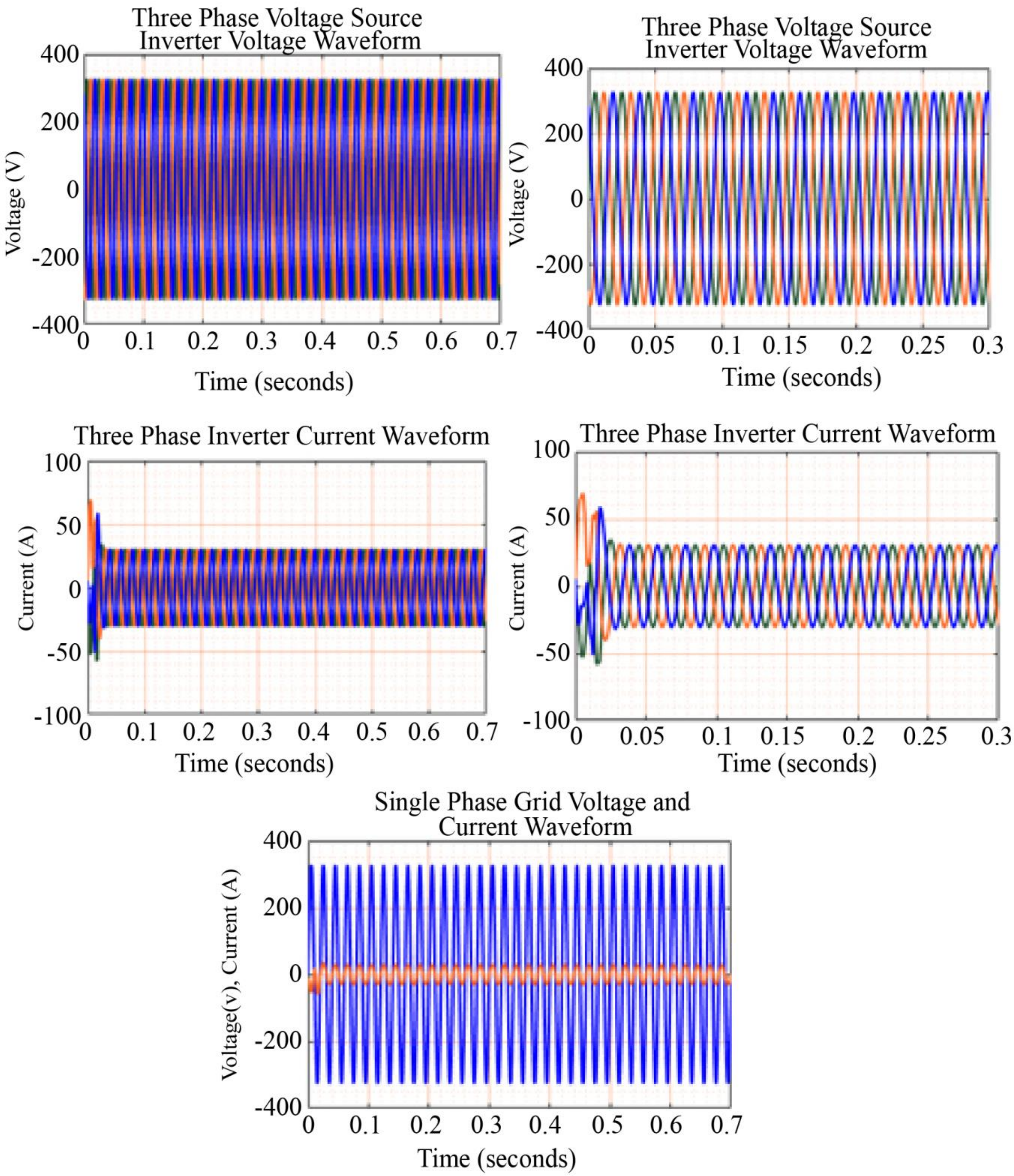

Fig. 15 Waveform of grid

Figure 15 represents the waveform of the grid with 20 KW power. The voltage of the grid is settled at a constant value of 330 V in the entire system. Also, the grid current is maintained at a constant value of 30 A throughout the system. Consequently, in phase grid voltage and current are 330 V, 30 A on the whole system.

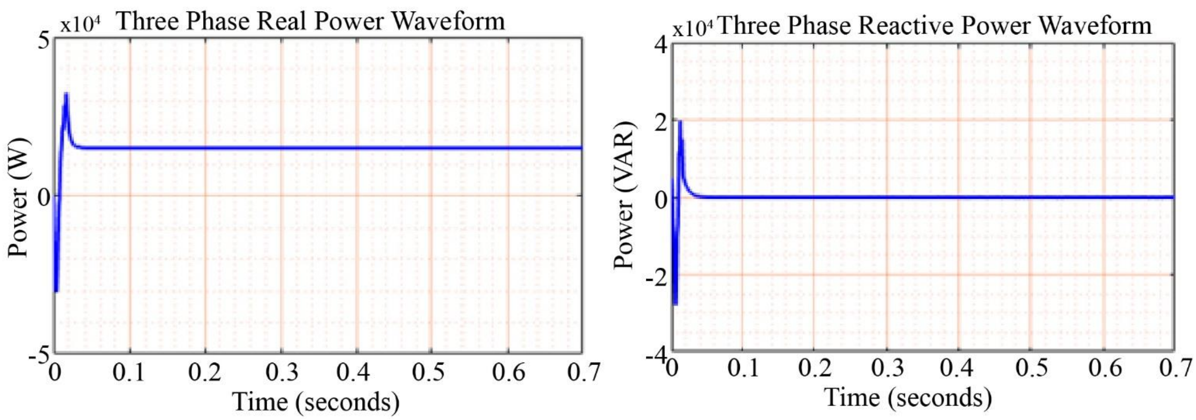

Fig. 16 Waveform of real and reactive power

The waveform of real and reactive power is presented in Figure 16. The real power is sustained at $1.5 \times 10^4 W$, representing the constant energy consumption while the reactive power is maintained at a value of $0 \times 10^4\ VAR$.

3.4. Case 2: Grid Power (10 kW)

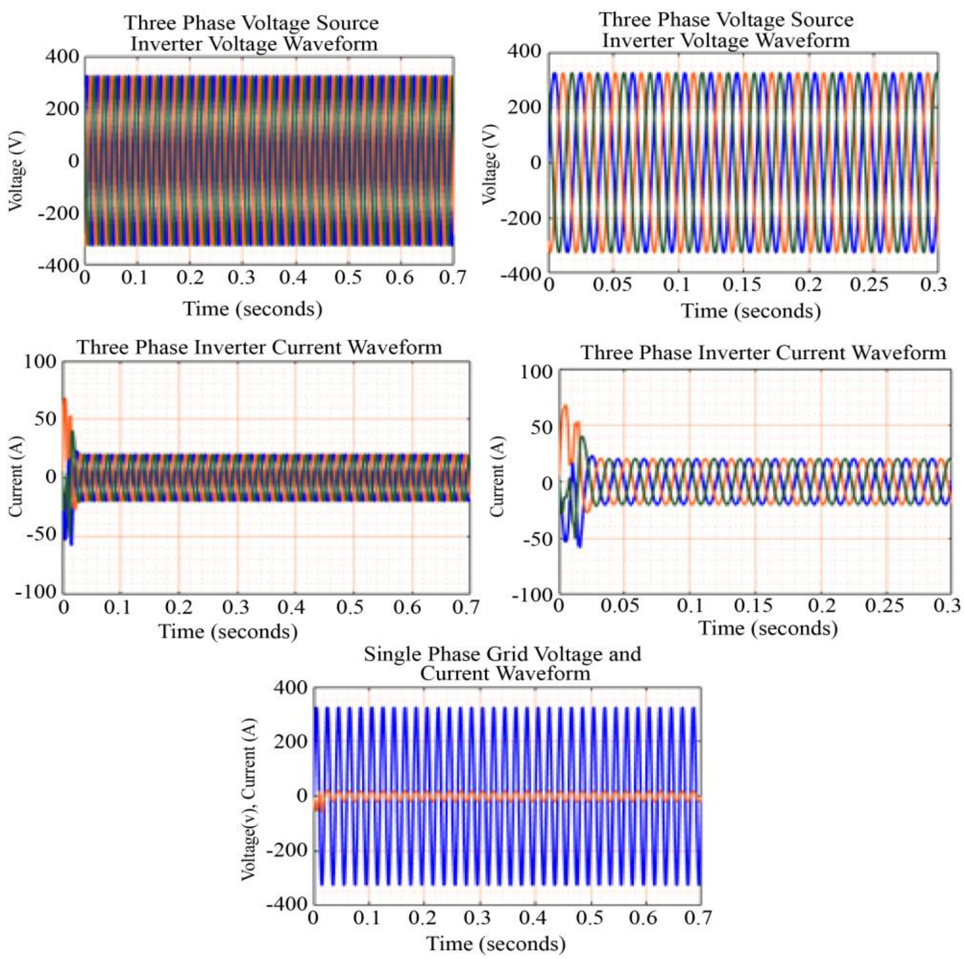

Fig. 17 Waveform of grid

Figure 17 indicates the waveform of the grid with 10 kW grid power. The stable value of 330 V is sustained for grid voltage. Similarly, a grid current is maintained a value of 30 A in the entire system. The in-phase grid voltage and current have stable values of 330 V 30 A throughout the system.

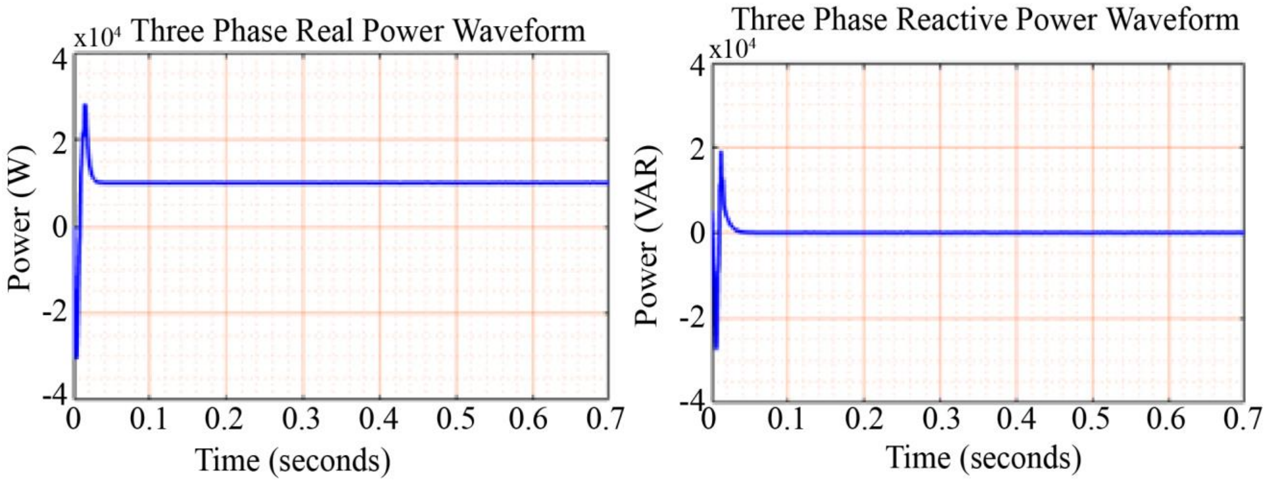

Fig. 18 Waveform of real and reactive power

The waveform of real and reactive power is represented in Figure 18. The real power is settled at a value of $1 \times 10^4 W$ whereas the reactive power is sustained at a lower value in the entire system.

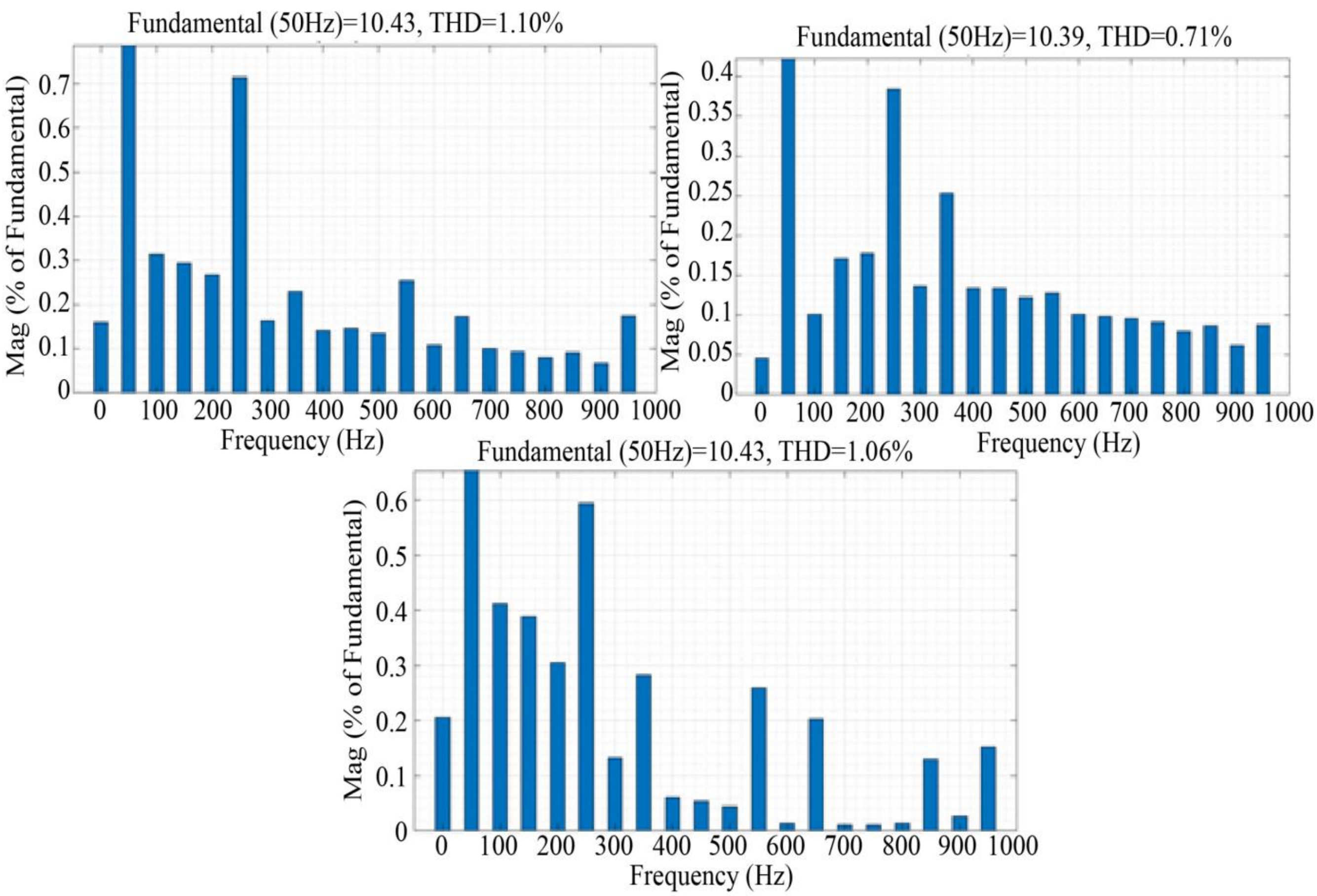

Fig. 19 Waveform of THD

Figure 19 displays the waveform of THD for the R, Y, and B phases. The Y phase has the lowest THD of 0.71% than the R (1.10 %) and B (1.06%) phases, representing enhanced power quality.

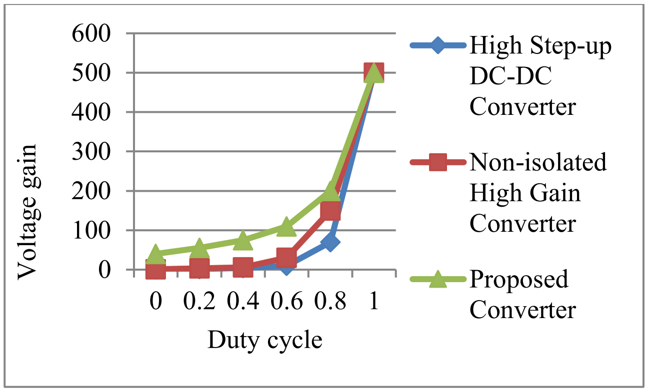

Fig. 20 Analysis of voltage gain

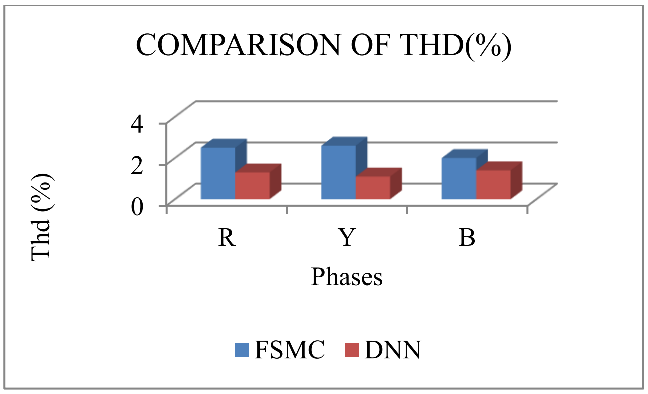

Fig. 21 Analysis of THD

Figure 20 compares the voltage gain for the designed converter, non-isolated high gain [25], and high step-up [24]. Compared to other converters, the created converter achieves the largest voltage gain, indicating that the system's overall effectiveness has been improved. This is attained through the integration of voltage multiplier stages and the careful design of switching control, contributing to improved conversion efficiency.

Figure 21 provides a comparative analysis of the Total Harmonic Distortion (THD) for the R, Y, and B phases with a Fuzzy Sliding Mode Controller (FSMC) [26] and DNN. The DNN controller has the lowest THD of $1.10\,\%, 0.71\%$ *and* 1.06% (R, Y, and B phases) than the FSMC approach, thereby minimizing THD across all three phases, making it a more effective approach for decreasing harmonic distortion compared to FSMC. The DNN controller allows generalization and optimization in real-time due to its training on a wide range of operating conditions. It maintains optimal control performance owing to its ability to continuously learn and adjust internal parameters.

Figure 22 shows the performance comparison between two approaches, Neural Network (NN) [27] and the proposed approach for grid current analysis across R, Y, and B phases. The NN approach has the highest grid current percentage among all phases, while the proposed method has a THD of $3.03\,\%, 3.29\,\%$ *and* $3.14\,\%$, indicating better efficacy. The proposed method is more effective in regulating grid current, thereby improving system performance.

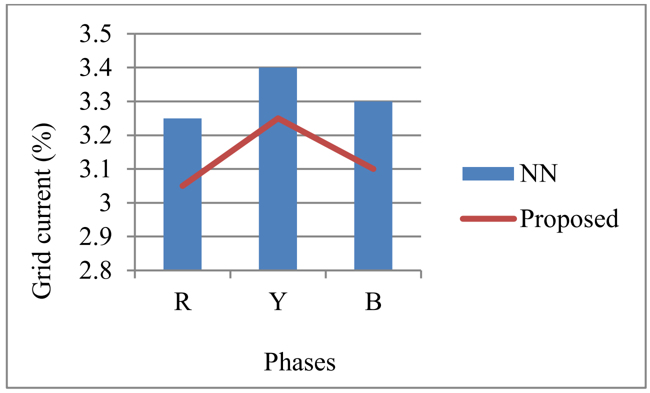

Fig. 22 Analysis of Grid current

Table. 2 Analysis of Grid current THD for Voltage Sag/Swell conditions

Grid current THD (%)			
Voltage Sag/Swell (%)		NN control [27]	Proposed
Voltage Sag	5	2.75	2.41
	10	2.9	2.76
	15	3.1	3.01
	20	3.4	3.32
	30	3.7	3.15
Voltage Swell	5	2.8	2.05
	10	2.97	2.34
	15	3.21	3.03
	20	3.39	3.17
	30	3.58	3.28

The analysis of grid current under varying voltage sag and swell conditions for NN and the proposed method is seen in Table 2. A proposed method consistently attains lower THD, emphasizing its effectiveness in handling both voltage sag and swell scenarios. This demonstrates the enhanced robustness and efficiency of the proposed approach in managing harmonic distortions during voltage disturbances.

4. Conclusion

To solve power quality issues, this research implements a novel DSTATCOM-based DNN controller. The DSTATCOM enhances the power factor by compensating for reactive power, which improves the efficacy of the power system and it delivers a fast response to transient disturbances that enhances the overall robustness of the power system. Subsequently, the DNN controller lessens the power quality concerns like voltage fluctuations, harmonics, and frequency deviations, leading to a more steady and efficient power supply. By exploiting an improved cascaded boost converter, the PV system's voltage is increased with high efficiency and voltage gain. Furthermore, the HHO optimized Fuzzy-MPPT technique effectively tracks the PV system's optimal power. To validate the efficiency of the implemented work, the introduced research is also applied in MATLAB/Simulink and compared to conventional topologies. Consequently, the outcomes indicate that the developed work attains better PQ with a lesser THD of 0.71%, ensuring that continuous power without PQ problems is supplied to load applications. However, computational complexity due to the hybridization of approaches is regarded as a major limitation since it leads to increased processing time. This is a major concern that has to be considered in future work.

References

[1] Chapala Shravani, RL. Narasimham, and G. Tulasi Ram Das, "Synergetic UPQC Application for Power Quality Enhancement in Microgrid Distribution System: SCSO Approach," *e-Prime-Advances in Electrical Engineering, Electronics and Energy*, vol. 10, 2024. [CrossRef] [Google Scholar] [Publisher Link]

[2] Eyad S. Oda et al., "Stochastic Optimal Planning of Distribution System Considering Integrated Photovoltaic-Based DG and DSTATCOM Under Uncertainties of Loads and Solar Irradiance," *IEEE Access*, vol. 9, pp. 26541-26555, 2021. [CrossRef] [Google Scholar] [Publisher Link]

[3] Amit Kumar, and Pradeep Kumar, "Power Quality Improvement for Grid-connected PV System Based on Distribution Static Compensator with Fuzzy Logic Controller and UVT/ADALINE-based Least Mean Square Controller," *Journal of Modern Power Systems and Clean Energy*, vol. 9, no. 6, pp. 1289-1299, 2021. [CrossRef] [Google Scholar] [Publisher Link]

[4] N.V. Vinay Kumar, and Tenepalli Gowri Manohar, "Meta Heuristic Algorithm Based Novel Dstatcom Architecture for Power Quality Improvement," *International Journal of Experimental Research and Review*, vol. 38, pp. 119-131, 2024. [CrossRef] [Google Scholar] [Publisher Link]

[5] L. Narayana Gadupudi et al., "Seven Level Voltage Source Converter Based Static Synchronous Compensator with a Constant DC-Link Voltage," *Applied Sciences*, vol. 11, no. 16, pp. 1-17, 2021. [CrossRef] [Google Scholar] [Publisher Link]

[6] Abdallah Fouad et al., "Enhancing Grid-Connected DFIG's LVRT Capability Using Dandelion Optimizer Based the Hybrid Fractional-Order PI and PI Controlled STATCOM," *IEEE Access*, vol. 12, pp. 120181-120197, 2024. [CrossRef] [Google Scholar] [Publisher Link]

[7] L. Narayana Gadupudi, "Recent Advances of STATCOM in Power Transmission Lines-A Review," *Turkish Journal of Computer and Mathematics Education (TURCOMAT)*, vol. 12, no. 3, pp. 4621-4626, 2021. [Google Scholar] [Publisher Link]

[8] L. Narayana Gadupudi, and Gudapati Sambasiva Rao, "7-Level Transformers Integrated Voltage Source Converter Based STATCOM for Voltage Profile Enhancement," *Solid State Technology*, vol. 63, no. 5, pp. 3134-3141, 2020. [Google Scholar] [Publisher Link]

[9] L.N. Gadupudi, Gudapati Sambasiva Rao, "9-Level VSC based STATCOM for Reactive Power Management and Voltage Stability Improvement," *Journal of Green Engineering*, vol. 10, pp. 10275-10288, 2020. [Google Scholar]

[10] Naeem Abas et al., "Power Quality Improvement Using Dynamic Voltage Restorer," *IEEE Access*, vol. 8, pp. 164325-164339, 2020. [CrossRef] [Google Scholar] [Publisher Link]

[11] Swapnil D. Patil et al., "Performance Enhancement of Modified Svc as a Thyristor Binary Switched Capacitor and Reactor Banks by using Different Adaptive Controllers," *Journal of King Saud University-Engineering Sciences*, vol. 35, no. 5, pp. 342-357, 2023. [CrossRef] [Google Scholar] [Publisher Link]

[12] Bharath Singh Jebaraj et al., "Power Quality Enhancement in Electric Arc Furnace Using Matrix Converter and Static VAR Compensator," *electronics*, vol. 10, no. 9, pp. 1-20, 2021. [CrossRef] [Google Scholar] [Publisher Link]

[13] C. Subramani, K. Dhineshkumar, and P. Palanivel, "Design and Implementation of 13 Levels Multilevel Inverter for Photovoltaic System," *Journal of Physics: Conference Series*, *National Conference on Mathematical Techniques and its Applications (NCMTA 18)*, Kattankulathur, India, vol. 1000, pp. 1-8, 2018. [CrossRef] [Google Scholar] [Publisher Link]

[14] Kanthapitchai Paul Joshua et al., "Energy Management of Solar Photovoltaic Fed Water Pumping System Based BLDC Motor Drive using NBO-SDRN Approach," *Electrical Engineering*, vol. 106, no. 3, pp. 3045-3059, 2024. [CrossRef] [Google Scholar] [Publisher Link]

[15] Chang-Hua Lin et al., "Design and Analysis of Novel High-Gain Boost Converter for Renewable Energy Systems (RES)," *IEEE Access*, vol. 12, pp. 24262-24273, 2024, [CrossRef] [Google Scholar] [Publisher Link]

[16] Vemparala Seshagiri Rao, and Kumaravel Sundaramoorthy, "Performance Analysis of Voltage Multiplier Coupled Cascaded Boost Converter with Solar PV Integration for DC Microgrid Application," *IEEE Transactions on Industry Applications*, vol. 59, no. 1, pp. 1013-1023, 2022. [CrossRef] [Google Scholar] [Publisher Link]

[17] K.S. Kavin et al., "A Novel KSK Converter with Machine Learning MPPT for PV Applications," *Electric Power Components and Systems*, pp. 1-19, 2024. [CrossRef] [Google Scholar] [Publisher Link]

[18] Asaad A.H. AlZubaidi et al., "Mppt Implementation and Simulation using Developed P&O Algorithm for Photovoltaic System Concerning Efficiency," *Bulletin of Electrical Engineering and Informatics*, vol. 11, no. 5, pp. 2460-2470, 2022. [CrossRef] [Google Scholar] [Publisher Link]

[19] Mahmoud N. Ali et al., "An Efficient Fuzzy-Logic Based Variable-Step Incremental Conductance MPPT Method for Grid-Connected PV Systems," *IEEE Access*, vol. 9, pp. 26420-26430, 2021. [CrossRef] [Google Scholar] [Publisher Link]

[20] K.S. Kavin, et al., "Improved BRBFNN-Based MPPT Algorithm for Coupled Inductor KSK Converter for Sustainable PV System Applications," *Electrical Engineering*, pp. 1-23, 2025. [CrossRef] [Google Scholar] [Publisher Link]

[21] Al-wesabi Ibrahim et al., "PV Maximum Power-Point Tracking using Modified Particle Swarm Optimization Under Partial Shading Conditions," *Chinese Journal of Electrical Engineering*, vol. 6, no. 4, pp. 106-121, 2020. [CrossRef] [Google Scholar] [Publisher Link]

[22] Ramesh Gugulothu, Bhookya Nagu, and Deepak Pullaguram, "A Computationally Efficient Jaya Optimization for Fuel Cell Maximum Power Tracking," *Energy Sources, Part A: Recovery, Utilization, and Environmental Effects*, vol. 44, no. 1, pp. 1541-1565, 2022. [CrossRef] [Google Scholar] [Publisher Link]

[23] Kun Xia, Yin Li, and Benjing Zhu, "Improved Photovoltaic MPPT Algorithm Based on Ant Colony Optimization and Fuzzy Logic under Conditions of Partial Shading," *IEEE Access*, vol. 12, pp. 44817-44825, 2024. [CrossRef] [Google Scholar] [Publisher Link]

[24] Kazem Varesi, Naser Hassanpour, and Saeid Saeidabadi, "Novel High Step-Up DC–DC Converter with Increased Voltage Gain Per Devices and Continuous Input Current Suitable for DC Microgrid Applications," *International Journal of Circuit Theory and Applications*, vol. 48, no. 10, pp. 1820-1837, 2020. [CrossRef] [Google Scholar] [Publisher Link]

[25] Hossein Gholizadeh, and Lazhar Ben-Brahim, "A New Non-Isolated High-Gain Single-Switch DC-DC Converter Topology with a Continuous Input Current," *Electronics*, vol. 11, no. 18, pp. 1-20, 2022. [CrossRef] [Google Scholar] [Publisher Link]

[26] Bomma Shwetha, G. Suresh Babu, and G. Mallesham, "Intelligent Solar PV Grid Connected and Standalone UPQC for EV Charging Station Load," *Results in Control and Optimization*, vol. 15, 2024. [CrossRef] [Google Scholar] [Publisher Link]

[27] Okech Emmanuel Okwako et al., "Neural Network Controlled Solar PV Battery Powered Unified Power Quality Conditioner for Grid Connected Operation," *Energies*, vol. 15, no. 18, pp. 1-18, 2022. [CrossRef] [Google Scholar] [Publisher Link]